Synthesis of [3 + 3] β-ketoenamine-tethered covalent organic frameworks (COFs) for high-performance supercapacitance and CO$_2$ storage

Ahmed F.M. EL-Mahdy [a,b], Ying-Hui Hung [a], Tharwat Hassan Mansoure [b,c,d],
Hsiao-Hua Yu [c,d,e], Yu-Shen Hsu [f], Kevin C.W. Wu [f,h,*], Shiao-Wei Kuo [a,g,*,**]

[a] Department of Materials and Optoelectronic Science, Center of Crystal Research, National Sun Yat-Sen University, Kaohsiung 80424, Taiwan
[b] Chemistry Department, Faculty of Science, Assiut University, Assiut 71516, Egypt
[c] Institute of Chemistry, Nanoscience and Technology Program, Taiwan International Graduate Program, Academia Sinica, Taipei 11529, Taiwan
[d] Department of Chemistry, National Taiwan University, Taipei 106, Taiwan
[e] Center for Emergent Functional Matter Science, National Chiao Tung University, Hsinchu 30010, Taiwan
[f] Department of Chemical Engineering, National Taiwan University, No. 1, Sec. 4, Roosevelt Rd., Taipei 10617, Taiwan
[g] Department of Medicinal and Applied Chemistry, Kaohsiung Medical University, Kaohsiung 807, Taiwan
[h] International Graduate Program of Molecular Science and Technology, National Taiwan University (NTU-MST), No. 1, Sec. 4, Roosevelt Road, Taipei 10617, Taiwan

ARTICLE INFO

ABSTRACT

We report three new β-ketoenamine-linked covalent organic frameworks (COFs) prepared through Schiff-base [3 + 3] polycondensations of 1,3,5-triformylphloroglucinol (TFP-3OHCHO) with three tris(aminophenyl)-presenting derivatives—featuring amino, carbazole, and pyridine units, respectively under solvothermal conditions. The resultant TFP-COFs possessed high BET specific surface area up to 686 m^2 g^{-1} and excellent crystallinity, which showed excellent electrochemical specific capacitances (up to 291.1 F g^{-1}) and CO$_2$ uptake efficiency up to 200 mg g^{-1} at 273 K. We propose the enhanced performance in supercapacitor and gas storage is owing to the conjugated enamine structures with redox-active triphenyl amino, carbazole, and pyridine moieties. In addition, we further investigate the formation mechanism of the spherical TFP-TPA COF by studying the morphological changes over time. The presence of more highly planar monomer units in the hexagonal structures of the resultant COFs led to stronger quadrupolar interaction with the included CO$_2$ molecules.

© 2019 Taiwan Institute of Chemical Engineers. Published by Elsevier B.V. All rights reserved.

1. Introduction

Supercapacitors (SCs) are attracting a lot of interest for their use as energy storage devices [1]. Among them, electric double-layer capacitors have particularly useful short charging and discharging times, long cycle lives, high power densities, wide-ranging working temperatures, and environmental friendliness [2–4]. In these types of devices, charge storage at the interface between the electrolyte and the electrode occurs through fast and reversible adsorption/desorption reactions [5]. Therefore, the electrode materials must have precise distributions of their pore size,

high thermal stability, and stable electrochemical behavior [6]. In this context, many advanced porous carbon-containing materials with suitable pore size distributions (e.g., activated carbon [7], porous nanocarbon [8], composite nanocarbon [9], porous graphene [10–12], graphene aerogels [13–15], and mesoporous carbon [16]) have been developed in attempts to improve their effective performance in supercapacitors. Doping such carbon materials with nitrogen atoms can enhance the efficiency of supercapacitors as a result of the pseudocapacitance effect offered by nitrogen atoms [17]. Because they contain amino moieties in the framework structures, particular crystalline networks, tailorable pore sizes, and amenability to different types of heteroatom doping, several porous polymer materials (e.g., covalent triazine-based frameworks [18–20], metal–organic frameworks [21,22], or covalent organic frameworks (COF) [23,24]) have been considered ideal materials for use as electrodes in supercapacitors. From the electrochemical perspective, COFs provide outstanding behavior within supercapacitors, with predictable pore parameters and ordered

structures, making them promising electrode materials for practical devices [25,26].

COFs can be constructed with atomically accurate integration of building blocks into continuous three-dimensional (3D) or simple two-dimensional (2D) structure, with ordered pores and periodic frameworks [27]. There is a major difference between general amorphous polymers and COFs: namely, that the distinguishing crystallinity of COFs is provided by reversible condensations that yield, for example, boronate, borazine, imine, triazine, and azo-dioxide linkages [28–31]. Considering that they can absorb high amounts of various gas molecules in ordered arrangements, with high thermal and chemical stabilities, COFs can display functions unlike those of many other porous materials [28,31–33]. On the whole, COFs are organic crystalline micro- and macro-porous materials possessing high degrees of porosity, constructed through various types of reversible covalent bonds [33,34]. Nevertheless, the most attractive characteristic of COFs is because their chemical structures could be controlled precisely, by varying their building blocks through organic synthesis, depending on application in mind [35,36]. To date, COFs have already been used widely, in catalysis [37–39], optoelectronics [40,41], gas storage [42–45], separation [46], drug delivery [47,48], environmental remediation [49], and energy storage [50,51]. The use of COFs in supercapacitors has, however, been limited by the poor oxidative and hydrolytic stabilities of the previously tested materials [31,52].

Recent studies have suggested that the supercapacitor efficiencies of COFs could be improved in two ways: (i) including a redox moiety in β-ketoenamine-linked COFs and (ii) adding metal ions in polyimine-based COFs. In the first approach, the incorporation of a redox-active moiety—for example, a 2,6-diaminoanthraquinone (DAAQ) or 2,5-diaminopyridine (DAP) unit—into the hexagonal backbone of the COF has indeed enhanced the supercapacitor efficiencies. For example, DeBlase et al. [25,26] prepared the first redox-efficient β-ketoenamine-linked COF (DAAQ-TFP COF) containing a 2,6-diaminoanthraquinone moiety in its structure, and found that the resultant DAAQ-BTA COF functionalized electrode exhibited good supercapacitor efficiency in H_2SO_4 as the electrolyte. Likewise, Lei and co-workers [53] prepared a DAAQ-BTA COF/graphene composite that exhibited good specific capacitance in KOH as the electrolyte. Furthermore, Khattak et al. [1] reported a redox-active COF (TaPa-Py COF) featuring 2,5-diaminopyridine (DAP) units, and found that the resulting electrode displayed faradaic behavior and high specific capacitance in H_2SO_4 as the electrolyte. Although these reported examples all featured good specific capacitance, the selection of redox-active moieties has been limited to pyridine and anthraquinone units. In the second approach polyimine-based COFs with metal ions (Co^{II}, Ni^{II}, Fe^{III}) in their cavities have been converted, under pyrolysis (900 °C, 4 h), into N-doped porous graphenes [54] that exhibited excellent specific capacitances in KOH as the electrolyte, making them potentially useful as electrodes for supercapacitors. Although the specific capacitances of these kinds of pyrolyzed COFs have been superior to those of redox-active COFs, their preparation has required harsh conditions and the resulting COFs, totally converted into graphene, have lost their crystallinity. Thus, there is still interest in the construction of highly electrochemically efficient COFs containing novel redox-active moieties.

We and others have previously prepared COFs possessing planar and/or nonplanar monomer building units in their structures [55–58]. In a recent study, we found that the planarity and rigidity of the building monomers played powerful role affecting the structure, crystallinity, packing, and applications for the corresponding COFs [55]. Furthermore, we found that the nitrogen content in the hexagonal structure of the COFs was strongly correlated with the CO_2 uptake efficiency of the resultant COFs [55,56]. Nevertheless, to the best of our knowledge, there have been no previous

studies of the effect of the planarity of the building monomers, while maintaining the same nitrogen atom content, on the applications of β-ketoenamine-linked COFs. As part of our ongoing research in the discovery of new redox-active moieties and the effects of monomer planarity on the applications of corresponding COFs, in this paper we report the use of three tris(aminophenyl) derivatives including TPA-3NH$_2$, Car-3NH$_2$, and TPP-3NH$_2$, exhibiting various degrees of planarity, as novel redox-active moieties for the construction of three novel β-ketoenamine-linked COFs (Scheme 1) through one-pot [3 + 3] polycondensations with 1,3,5-triformylphloroglucinol (TFP-3OHCHO). Because the resultant β-ketoenamine-linked COFs exhibited excellent crystallinity and thermal stability, we examined their suitability for use in supercapacitor and for CO_2 uptake.

2. Result and discussion

2.1. Materials characterization

In order to prepare new β-ketoenamine-linked COFs with high-performance supercapacitor and excellent CO_2 uptake and study the role of linker's planarity on their properties and applications, we synthesized three TFP COFs—TFP-TPA, TFP-Car, and TFP-TPP COFs—through one-pot [3 + 3] polycondensations of TFP-3OHCHO (Figs. S1–S3) with TPA-3NH$_2$ (Figs. S4–S6), Car-3NH$_2$ (Figs. S7–S9), and TPP-3NH$_2$ (Figs. S10–S12) as novel redox-active and flexible tris(aminophenyl) building monomers (Scheme 1). Their syntheses were performed under solvothermal conditions using mesitylene and dioxane (1/1) as a co-solvent over 3 days at 120 °C, in the presence of 9% of acetic acid (6 M) as the catalyst. The obtained TFP-COFs were insoluble at room temperature, and even at high temperatures, in most organic solvents such as tetrahydrofuran, dioxane, acetone, dichloromethane, DMF or DMSO.

Table S1 presents the energy-minimized structures and optimized geometries of these tris(aminophenyl) building monomers, calculated using density functional theory (DFT) at the B3LYP/6-311 G (d,p) level. These theoretical calculations revealed that TPP-3NH$_2$ was the most planar of these building monomers, with Car-3NH$_2$ also having a more planar structure than TPA-3NH$_2$. We used elemental analysis, FTIR, and solid state NMR spectroscopy to confirm the formation of the corresponding TFP-COFs. The elemental analyses of TFP-TPA, TFP-Car, and TFP-TPP COFs provided C atom contents of 69.94%, 65.10%, and 66.30%, respectively; N atom contents of 10.72%, 10.51%, and 9.72%, respectively; and H atom contents of 4.90%, 4.77%, and 5.53%, respectively (Table S2), in good agreement with the theoretical values. The FTIR spectrum of TFP-3OHCHO was characterized by the strong broad absorption at 3453 cm^{-1} for phenolic-OH groups as well as two sharp signals at 1641 and 1432 cm^{-1} for CH=O and C=C units (Figs. S13–S15).

FTIR spectra of the tris(aminophenyl)-presenting monomers featured signals at 3406–3207 cm^{-1} for the amino NH$_2$ units, at 1620–1603 cm^{-1} for the bending of the N–H units, and at 1519–1504 cm^{-1} for aromatic C=C stretching (Figs. S13–S15). FTIR spectra of the TFP-COFs lacked any of the signals for the CH=O groups of the free TFP-3OHCHO monomer or the amino NH$_2$ groups of the free tris(aminophenyl) monomers, confirming their complete consumption. The appearance of a broad peak at 3442–3414 cm^{-1} for the NH units, as well as peaks at 1619–1610 cm^{-1} for C=O units, 1519–1448 cm^{-1} for conjugated C=C units, and 1261–1235 cm^{-1} for C–N units, confirmed that the C=O groups were present in the keto form and that the imino C=N linkers, formed through Schiff base condensation, had tautomerized into the enamine form (Figs. S13–S15). In other words, our synthesized TFP-COFs existed in keto-enamine form, stabilized through a large number of strong hydrogen bonds between the C=O groups and NH groups [25,26,28,59].
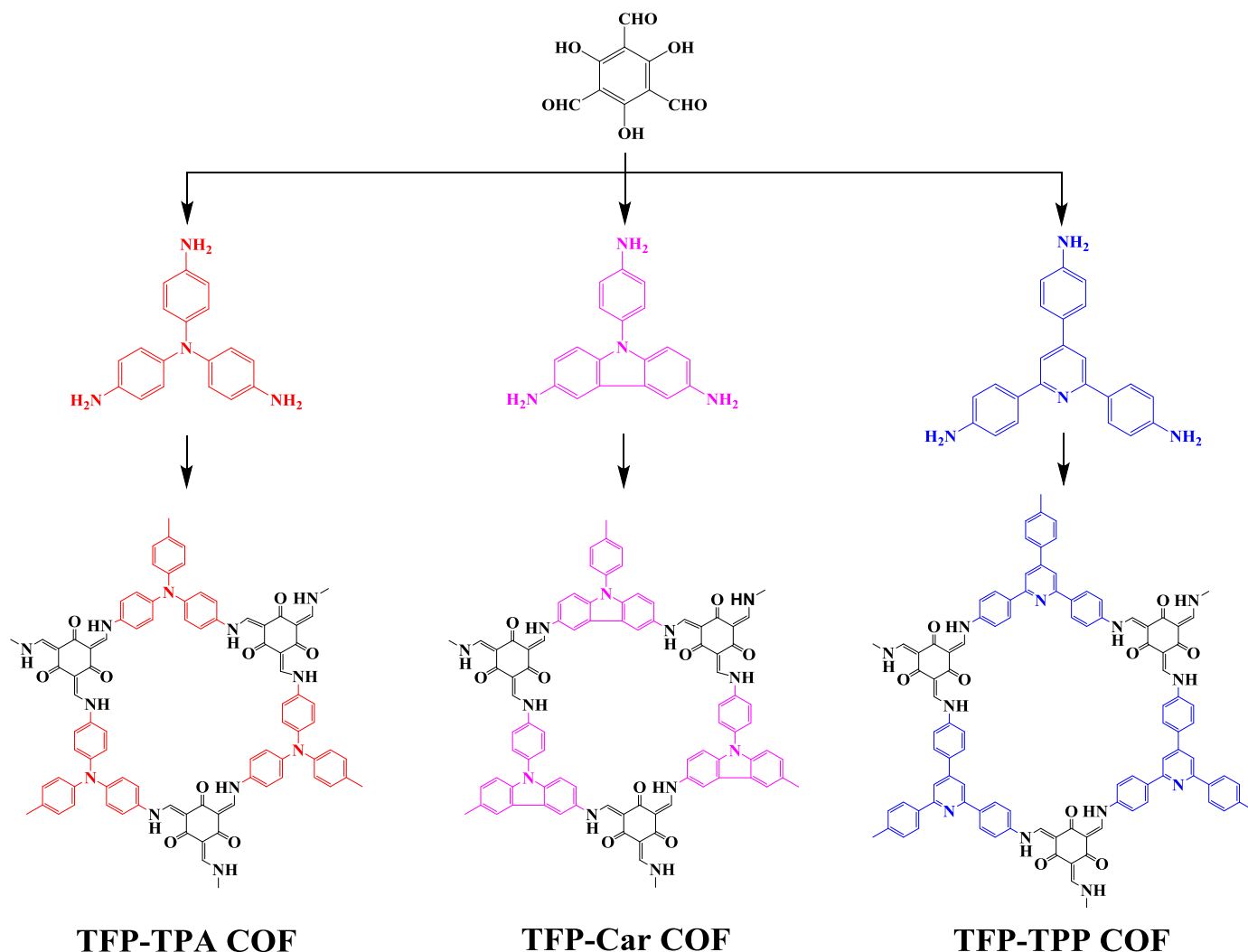
Scheme 1. Synthesis of three β-ketoenamine-linked COFs—the TFP-TPA, TFP-Car, and TFP-TPP COFs—from TFP-3OHCHO and tris(aminophenyl) derivatives having different degrees of planarity.

Solid state ^{13}C NMR spectroscopy confirmed the existence of the keto-enamine form. The ^{13}C NMR spectrum of TFP-3OHCHO featured a signal at 192.06 ppm for CH=O carbon and a signal at 173.58 ppm for C–OH carbon atoms (Fig. S2); the latter disappeared after the polycondensations with the tris(aminophenyl) building monomers to form TFP-COFs. Solid state ^{13}C NMR spectra of the TFP-COFs featured signals at 191.96–191.56 ppm for C=O units and other distinguishing signals at 154.42–153.29 and 114.62–114.28 ppm for the enamine (=C–NH) and α-enamine (C=C) carbon atoms, consistent with the formation of β-ketoenamine-linked COFs (Fig. 1 and S16–S18).

We used thermogravimetric analysis (TGA) to investigate the thermal stabilities of our new β-ketoenamine-linked COFs. Under a N$_2$ atmosphere, the TFP-COFs displayed high degrees of thermal stability up to a temperature of approximately 475 °C (Table S3 and Fig. S19). Considering the 10% weight loss (T_{d10}) and the onset temperature (T_{onset}), and the char yield as standards, we found that the TFP-TPP COF, constructed from the most planar monomer TPP-3NH$_2$, exhibited the highest thermal stability; its values of T_{d10} of 475 °C and T_{onset} of 489 °C (char yield: 51%) were slightly higher than those of TFP-Car COF (469 and 487 °C, respectively; char yield: 56%). On the other hand, TFP-TPA COF, constructed from the least planar monomer TPA-3NH$_2$, was the least thermally stable TFP-COF, with values of T_{d10} of 457 °C and T_{onset} of 477 °C (char yield: 52%). Thus, the planarity of the building linkers had a signif-

icant effect on the thermal stability of the obtained COFs, with a more planar monomer producing a more thermally stable COF.

To understand the permanent porosity and crystallinity of these new TFP-COFs, we measured their powder X-ray diffraction (XRD) and N$_2$ sorption behavior (Fig. 2). The XRD patterns of TFP-TPA, TFP-Car, and TFP-TPP COFs revealed high degrees of crystallinity, with ordered hexagonal 2D honeycomb-type frameworks (Fig. 2(a) and S20–S22). TFP-TPA COF exhibited the sharp peak at $2\theta = 6.81°$, which we attribute to the (100) reflection, in addition to other two peaks at $2\theta = 11.80$ and 13.96°, corresponding to (210) and (310) reflections, respectively. A broad peak at $2\theta = 20.41°$ attributed to the (001) reflection, which was caused by strong π-stacking between the 2D interlayers of this COF. The XRD pattern of TFP-Car COF with a series of peaks at values of 2θ of 7.48, 11.87, 14.11, and 22.16°, which we assign to the (100), (210) (310) and (001) reflections, respectively. Furthermore, TFP-TPP COF provided a sharp XRD peak at $2\theta = 4.89°$, accompanied by three minor peaks at $2\theta = 8.38$, 12.57, and 22.38°, also corresponding to the reflections of (100), (210), (310), and (001). The Bragg equation ($n\lambda = 2d\sin\theta$) could be calculated the average d-spacings between the (100) COF planes (d_{100}) and the π-interlayer distances between the 2D sheets of the COF planes; for TFP-TPA, TFP-Car, and TFP-TPP COFs, the values of d_{100} are 1.0, 1.1, and 1.6 nm, respectively, and the π-interlayer distances are 3.7, 3.5, and 3.4 Å, respectively (Table S4). Through simulations, we obtained the experimental XRD
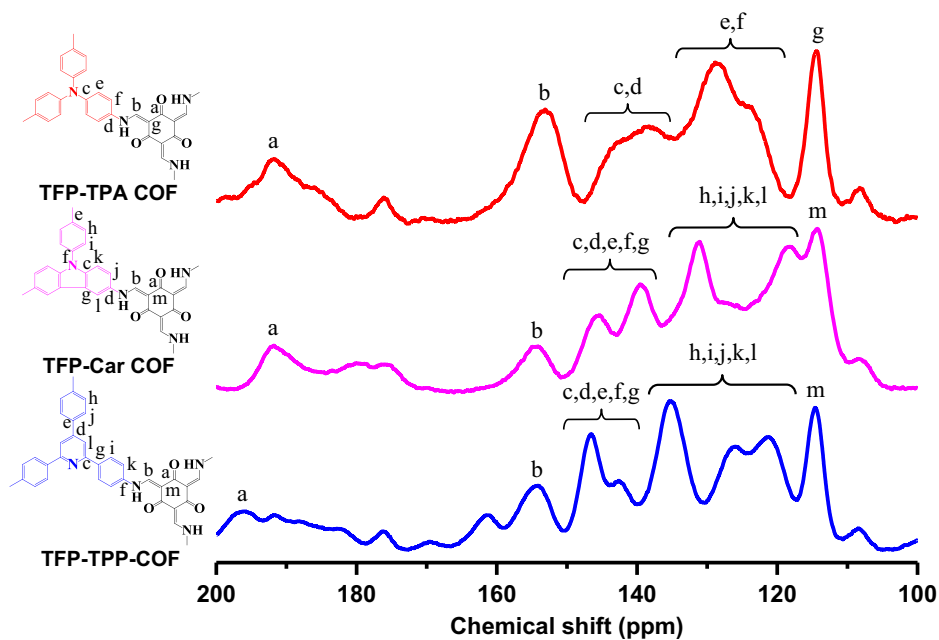
Fig. 1. Solid state ^{13}C NMR spectra of the TFP-TPA, TFP-Car, and TFP-TPP COFs.
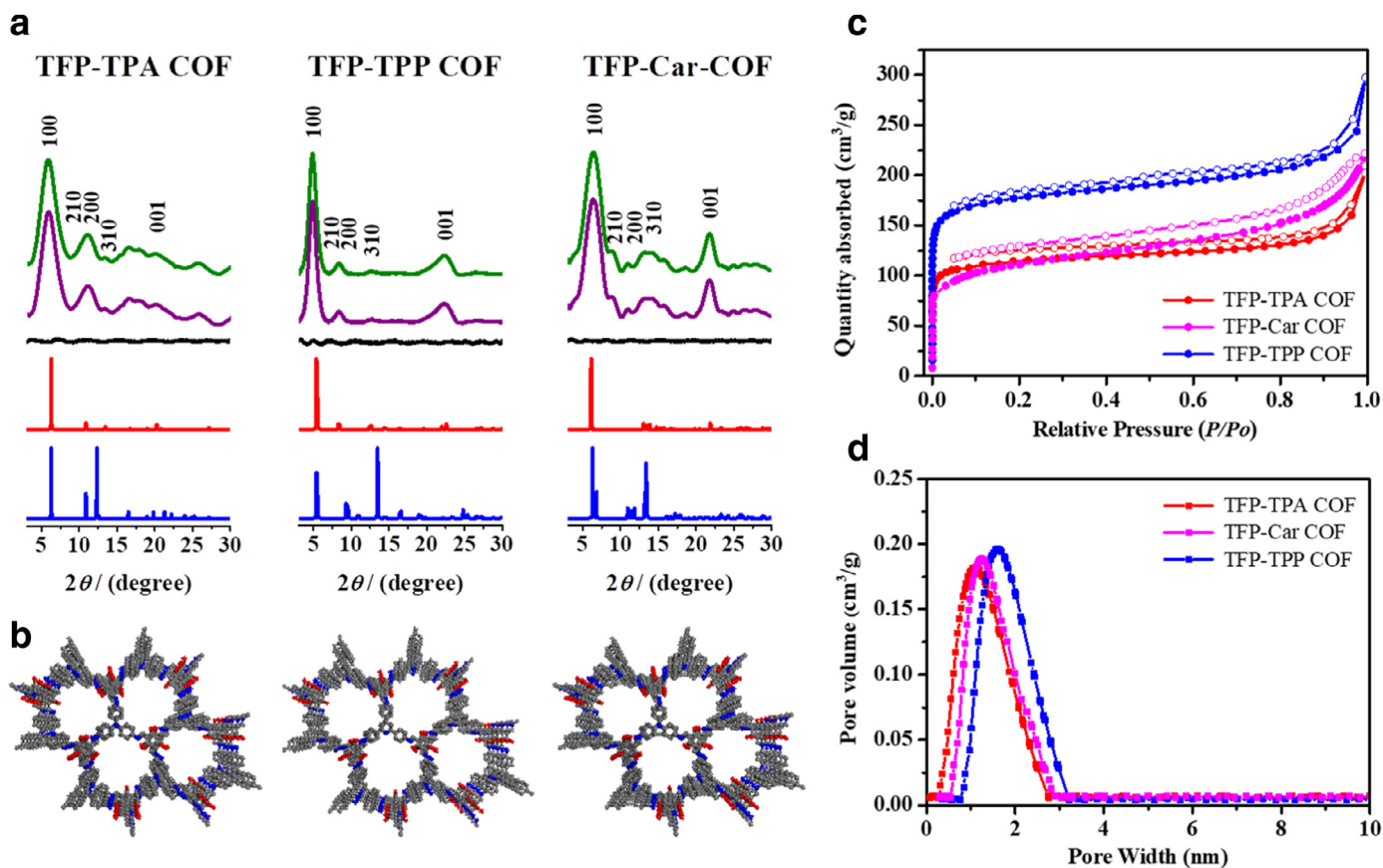

Fig. 2. (a) PXRD patterns of TFP-TPA, TFP-Car, and TFP-TPP COFs: experimental patterns (green), simulated patterns (purple) from Rietveld refinement, the difference between the measured and simulated patterns (black), and the calculated patterns from A–A (red) and A–B (blue) stacking. (b) 3D-space models of the TFP-TPA, TFP-Car, and TFP-TPP COFs obtained using A–A stacking crystalline structures [C (gray); N (blue), and O (red) atoms]. (c) N$_2$ adsorption (●) and desorption (○) isotherms measured at 77 K and (d) pore size distributions of TFP-TPA, TFP-Car, and TFP-TPP COFs. (For interpretation of the references to color in this figure legend, the reader is referred to the web version of this article.)
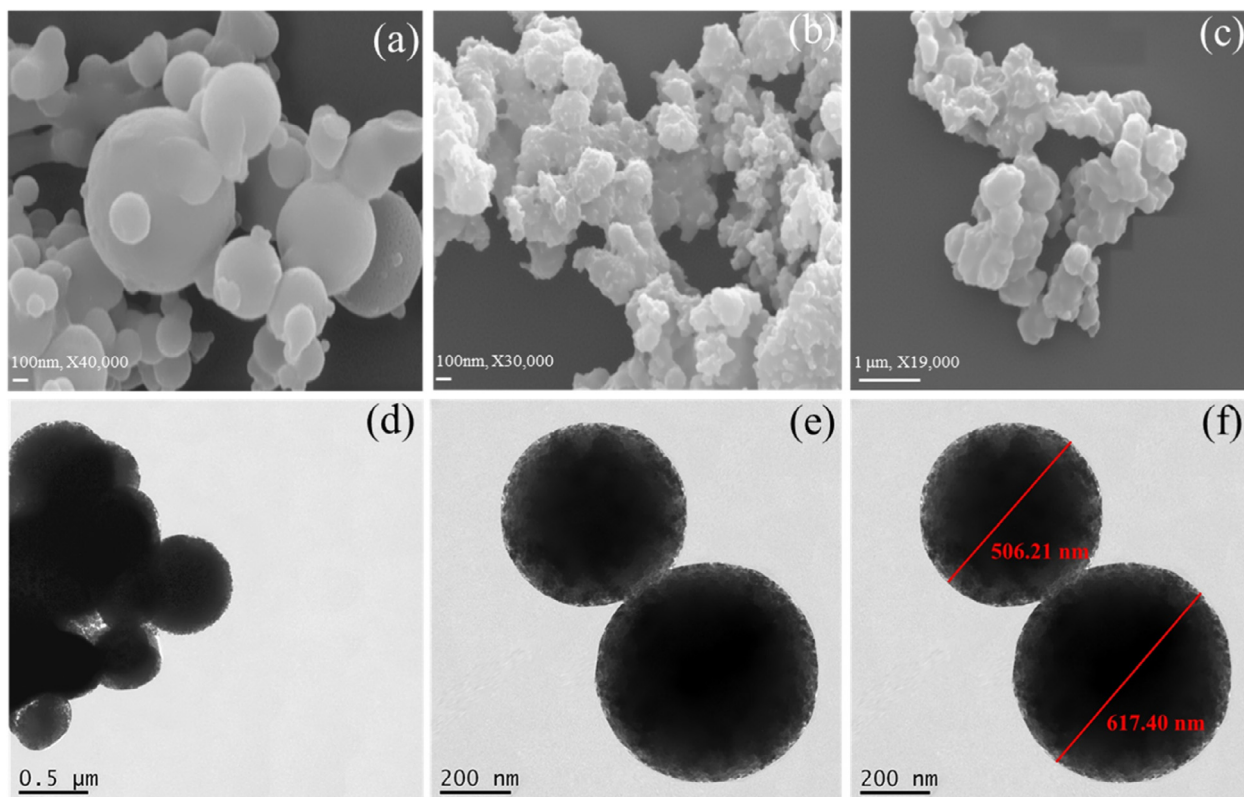
Fig. 3. (a–c) FE-SEM images of (a) TFP-TPA, (b) TFP-Car, and (c) TFP-TPP COFs. (d–f) TEM images of the spherical TFP-TPA COF, recorded at various magnifications.
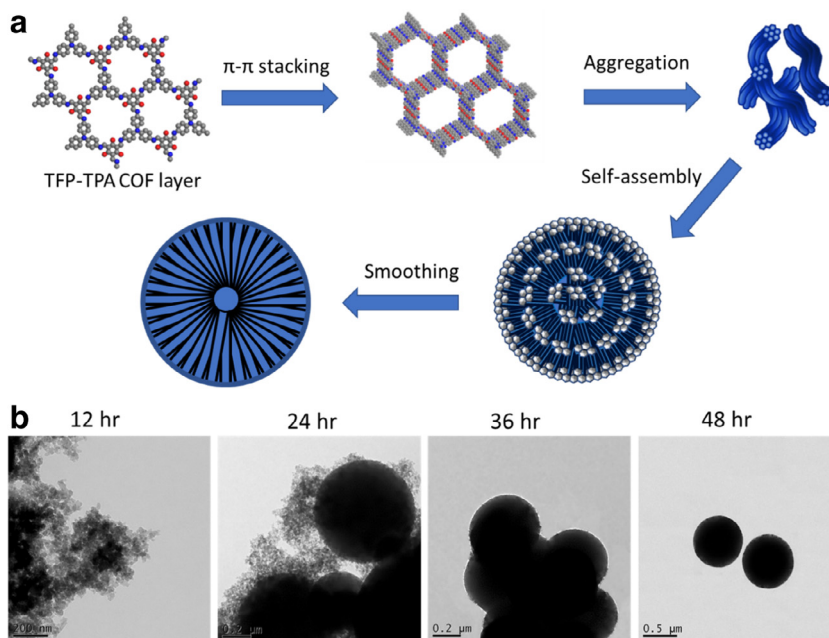

Fig. 4. (a) Schematic representation of the formation mechanism of the spherical TFP-TPA COF. (b) TEM images of TFP-TPA COF, recorded after various reaction time.

pattern for TFP-TPA, TFP-Car, and TFP-TPP COFs (Fig. 2(a), green curve) that was consistent with the theoretical pattern by using the Pawley refinement (Fig. 2(a), purple curve), as evidenced by only slight differences (Fig. 2(a), black curve). To further study the unit cell parameters and the layer conformations of our TFP-COFs, the Material studio program was used to construct eclipsed A–A stacking and staggered A–B stacking models for TFP-TPA, TFP-Car, and TFP-TPP COFs (Fig. 2(b), Tables S5–S7). The experimental XRD

pattern was matched with the simulated pattern for the eclipsed A–A stacking model (Fig. 2(a), red curve), but differed significantly from those for the staggered A–B stacking model (Fig. 2(a), blue curve).

Furthermore, the following parameters were provided by the unit cells of the eclipsed AA-stacking models: for TFP-TPA COF, $a = b = 16.22$ Å, $c = 4.17$ Å, $\alpha = \beta = 90°$, and $\gamma = 120°$ (Figs. S23 and S24, Table S8); for TFP-Car COF, $a = 13.79$ Å, $b = 16.90$ Å,

$c = 3.84$ Å, $\alpha = \beta = 90°$, and $\gamma = 120°$ (Figs. S25 and S26, Table S9); and for TFP-TPP COF, $a = 20.67$ Å, $b = 21.77$ Å, $c = 3.55$ Å, $\alpha = \beta = 90°$, and $\gamma = 120°$ (Figs. S27 and S28, Table S10). These data revealed that the degree of planarity of the tris(aminophenyl) linkers controlled the crystallinity of the resultant COFs; increasing the linker's planarity increased the d_{100} value and decreased π-interlayer distance between the 2D sheets of these produced COFs.

To determine the permanent porosity of these TFP-COFs, we measured the N_2 adsorption/desorption isotherms of the TFP-TPA, TFP-Car, and TFP-TPP COFs at 77 K (-196.15 °C) (Fig. 2(c)). The adsorption/desorption curves of these COFs were type I isotherm, due to the microporous materials. The three TFP-COFs showed large N_2 adsorption in the low relative pressure range ($P/P_0 = 0$–0.1 bar) followed by a tenuous increase in the pressure range ($P/P_0 = 0.1$–0.9 bar), then again large N_2 adsorption in the pressure range ($P/P_0 = 0.9$–1.0 bar). The N_2 desorption behavior of the three COFs exactly similar than their N_2 adsorption behavior except that for TFP-Car COF. the amount of N_2 desorption of TFP-Car COF is slightly less than that for N_2 adsorption at the same relative pressure, indicating the TFP-Car COF is stronger bonding to nitrogen atoms than other TFP-TPA and TFP-TPP COFs. The Brunauer–Emmett–Teller (BET) surface areas of TFP-TPA, TFP-Car, and TFP-TPP COFs, determined from their adsorption/desorption curves, were 457, 362, and 686 m^2 g^{-1}, accompanied by pore volumes of 0.28, 0.34, and 0.35 cm^3 g^{-1}, respectively (Table S4). In addition, we used non-local DFT to determine the pore size distribution of TFP-TPA, TFP-Car, and TFP-TPP COFs, revealing pore diameters of approximately 1.1, 1.2, and 1.6 nm, respectively (Table S4).

We used transmission electron microscopy (TEM) and field-emission scanning electron microscopy (FE-SEM) to investigate the morphologies of these COFs. After the liquid exfoliation in EtOH, the low-magnification TEM images of TFP-TPA, TFP-Car, and TFP-TPP COFs exhibited the ordered rhomboidal networks (Fig. S29). FE-SEM images of TFP-Car and TFP-TPP COFs revealed the assembly of uniformly distributed and loose blocks, while that of TFP-TPA COF revealed, interestingly, that it had assembled into a dark homogenous spherical structure (Fig. 3(a)–(c)). We used TEM to further investigate the spherical nature of the TFP-TPA COF. As displayed in Fig. 3(d)–(f), TEM image of TFP-TPA COF confirmed the spherical structure of this COF, and statistical analysis provided an average value for the diameters of the spheres of 500–600 nm. The majority of these spheres were present as bundles, but we observed some separated spheres, possibly resulting during the liquid sonication applied for 1 h during sample preparation. The formation of the spherical TFP-TPA COF presumably arose from the non-planarity of the tris(aminophenyl) building monomer TPA-$3NH_2$. Thus, as we had reported previously, the degree of planarity of the building monomers can have a major effect on the COFs morphology.

2.2. Formation mechanism

We examined the mechanism behind the formation of the spheres of TFP-TPA COF by studying the morphological changes of this COF at different time during its formation. For this study, TFP-TPA COF was synthesized under conditions similar to those described above, but at those particular points in times the reaction was quenched through removing reaction tube from oil bath and then cooling to room temperature. These isolated COFs were washed with acetone several times, followed by THF, before subjecting them to TEM imaging (Fig. 4(b)). The TFP-TPA COF constructed from the most nonplanar tris(aminophenyl) monomer TPA-$3NH_2$ formed the morphology of the isolated sample after 12 h. TEM image at this time exhibited the aggregation from small ribbon-like crystallite with average heights of 45–60 nm and average lengths of 140–200 nm (Fig. 4(b)). We attribute the
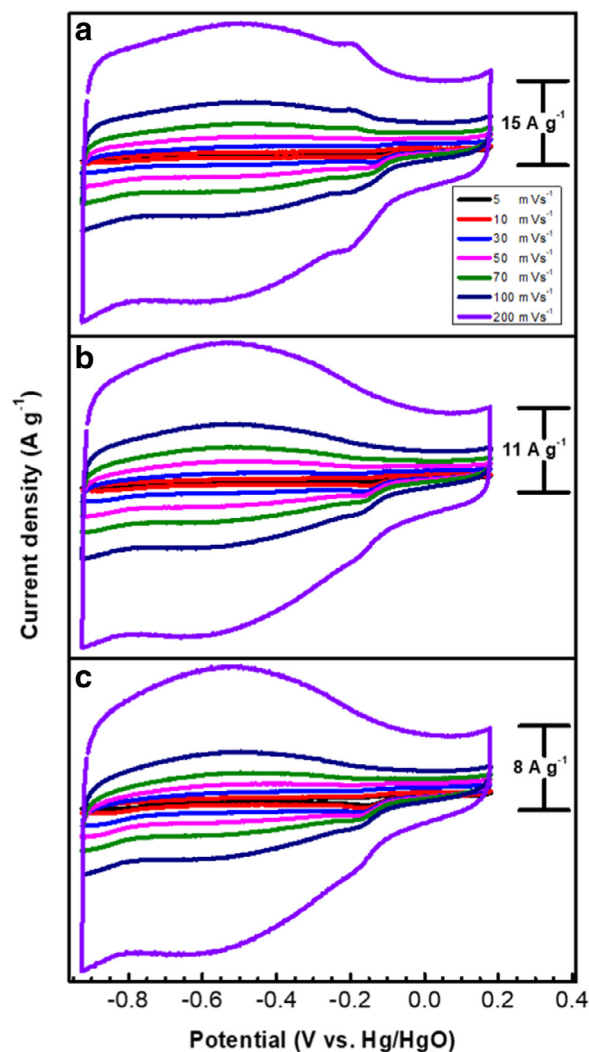

Fig. 5. Cyclic voltammograms, recorded at various scan rates in 1 M KOH, of the (a) TFP-TPA, (b) TFP-TPP, and (c) TFP-Car COFs.

formation of these kinds of crystallites to the strong π-stacking between the layers of TFP-TPA COF along the c-direction (Fig. 4(a)). These crystallites had self-assemble behavior after 24 h, to yield dark and dense spherical structures. Higher-magnification image (Fig. 4(b)) exhibited that individual crystallites had been used as the building blocks of the spheres; they were still evident on the outer shell of spheres. Interestingly, TEM images of isolated compound after 36 h revealed complete spherical structures with smooth outer shells (Fig. 4(b)). These smooth shells could be attributed to condensation reactions between the terminal amino and aldehydic groups of the crystallite surfaces.

It has been reported previously that the smooth surfaces of such spheres require the crystallites present on the sphere's surface to reacted among themselves through two different (*e.g.*, amino and aldehydic) terminal groups [56]. TEM images of isolated samples after 48 h also exhibited smooth spheres (Fig. 4(b)), suggesting that the actual time for forming the crystalline TFP-TPA COF was 36 h. Previously, we have reported the transformation of a spherical COF from dark smooth spheres into hollow spheres under the control of inside-out Ostwald ripening, in which crystallites at the inner center, having energy higher than those on the shell, migrated to the outer shell to minimize its surface energy [60,61]. For our β-ketoenamine-linked COF, however, the restricted migration of the crystallites of the TFP-TPA COF from the inner center
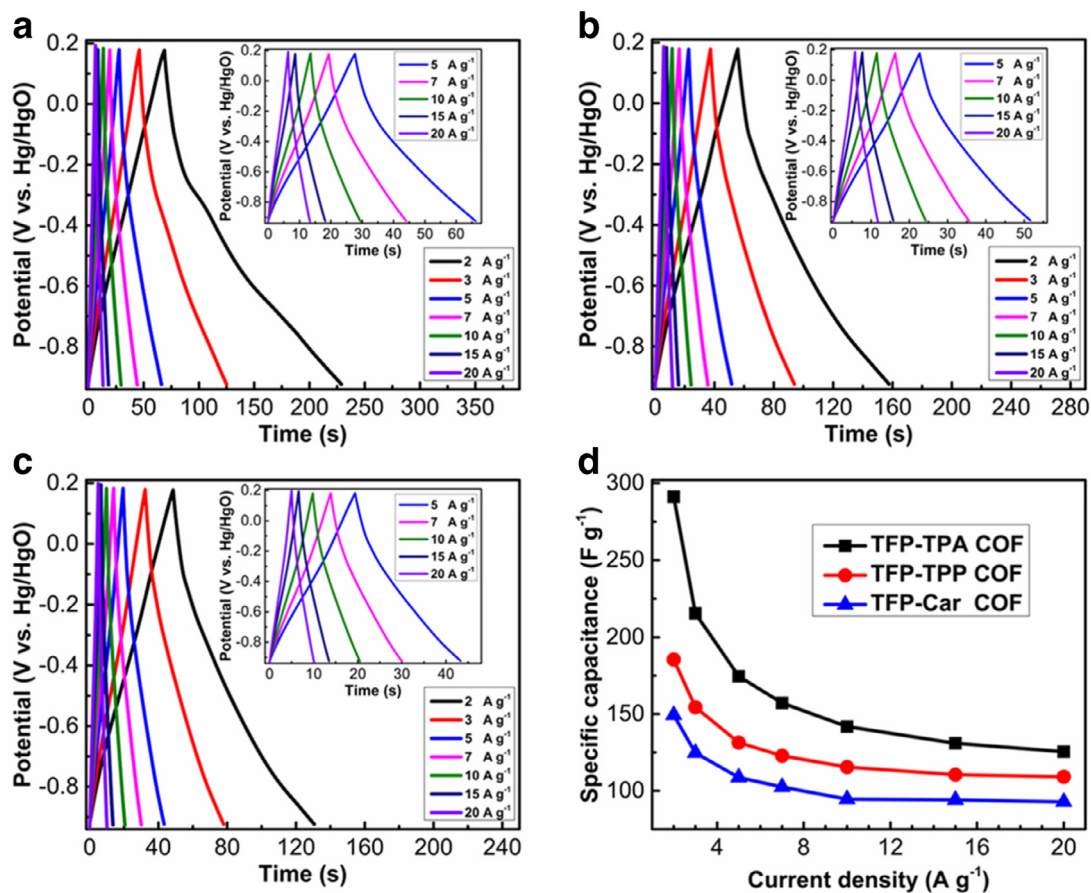
Fig. 6. (a–c) GCD profiles, recorded at various current densities in 1 M KOH, of the (a) TFP-TPA, (b) TFP-TPP, and (c) TFP-Car COFs. (d) Corresponding specific capacitances measured at the various current densities.

to the outer shell presumably arose from strong hydrogen bonding between these crystallites, thereby minimizing their energy in the inner center. Thus, the TFP-TPA COF maintained its morphology as dark spheres, without transformation into hollow spheres. Moreover, during the synthesis of the TFP-TPA COF, we also recorded XRD patterns of these samples isolated at various reaction time (Fig. S30). The crystallinity of each sample was evident, even after the shortest reaction time (12 h), suggesting that the aggregation, assembly, and smoothing of these COF crystallites did not disrupt the ordered internal structure for TFP-TPA COF.

2.3. Supercapacitor applications

To investigate the applicability of our β-ketoenamine-linked COFs, we measured their supercapacitor performance and CO_2 uptake efficiencies. We examined the electrochemical performance of our three TFP-COFs samples through cyclic voltammetry (CV) and galvanostatic charge–discharge (GCD) measurements by the three-electrode system in 1 M KOH aqueous solution. Fig. 5 displays the CV curves of these COFs, recorded with various sweep rates. These CV curves of these three TFP-COFs have rectangular-like shape with the appearance of humps, suggesting that the capacitive response originated from a combination of pseudocapacitance and electric double-layer capacitance (EDLC), which arose from the presence of the N and O heteroatoms [62,63]. In addition, the three COF samples possessed redox-active groups—amino [55,64], pyridine [1], and carbazole [65] units—in their structural backbones, inducing them to undergo reversible redox processes at a low sweep rate of 5 mV s^{-1} in the potential window from +0.18 to –0.92 V (Fig. S31). The peak separation between the processes of oxidation and

reduction was quite small, suggesting rapid transfer of electrons between the GC electrode and the COFs [24]. Moreover, the shape of the CV curve was retained well, but the current density increased, upon increasing the sweep rate (Fig. 5), suggesting facile kinetics and good rate capability [66].

Fig. 6 presents the GCD curves of TFP-COFs, recorded at various current densities. These GCD curves possessed triangular shapes with a slight bend, indicating the characteristics of both heteroatom-derived EDLC and pseudocapacity (derived from the presence of N and O atoms) [7,62,63]. The discharging time of the TFP-TPA COF was longer than those of the TFP-TPP COF and TFP-Car COFs (Fig. 6(a)–(c)), suggesting that the capacitances of TFP-TPA COF were larger than TFP-TPP and TFP-Car COFs. Fig. 6(d) presents the specific capacitances determined from GCD curves by using Eq. (S1). At a current density of 2 A g^{-1}, the TFP-TPA COF exhibited an excellent specific capacitance of 291.1 F g^{-1}, which was decreased to 125.5 F g^{-1} when the current density increased to 20 A g^{-1}. Although TFP-TPP COF possessed the highest surface area (686 m^2 g^{-1}) and a greater pore volume (0.35 cm^3 g^{-1}), it exhibited a specific capacitance smaller than that of the TFP-TPA COF. We ascribe this behavior to the higher N atom content of the TFP-TPA COF—evidenced from the elemental analysis data (Table S2)—increasing the number of active sites for the redox reactions and, thereby, contributing to the pseudocapacitive behavior of the electrode [67]. In addition, the spherical morphology of the TFP-TPA COF could provide the electrolytes with readier access to the electrode surface [68]. Khattak et al. prepared a TaPa-Py COF having capacitances of 209 F g^{-1} at 0.5 A g^{-1} and 164 F g^{-1} at 5 A g^{-1}. Furthermore, they prepared a DAAQ-TFP COF displaying the capacitance of 48 ± 10 F g^{-1} at 0.1 A g^{-1}, which was stabilized
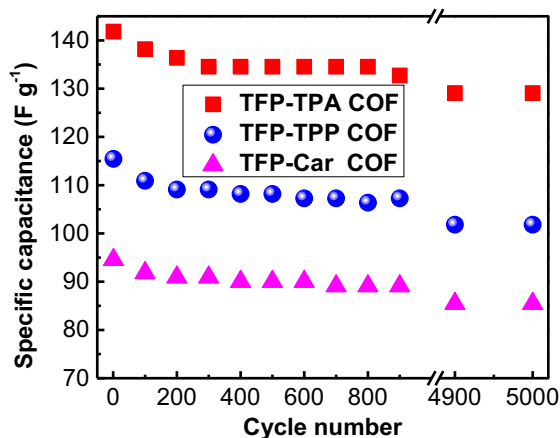
Fig. 7. Cycling performance of the TFP-COFs at a current density of 10 A g^{-1}.

at 40 ± 9 F g^{-1} after 10 cycles, and did not decrease significantly even after 5000 cycles [25]. Most recently, our group reported the Car-TPA, Car-TPP, and Car-TPT COFs with capacitances of 13.6, 14.5, and 17.4 F g^{-1}, respectively, at 0.2 A g^{-1} [56]; we also prepared TPA-COF-1, TPA-COF-2, TPA-COF-3, TPT-COF-4, TPT-COF-5, and TPT-COF-6 displaying capacitances of 51.3, 14.4, 5.1, 2.4, 0.34, and 0.24 F g^{-1}, respectively, at 0.2 A g^{-1} [55].

Table S11 summarizes the corresponding specific surface areas and specific capacitances. We tested the durability of these TFP-COFs by cycling over 5000 times at 10 A g^{-1} (Fig. 7). Significantly, the TFP-TPA COF displayed superior cycling stability, with a decrease in its specific capacitance from 141.8 to 129.1 F g^{-1} after 5000 cycles, corresponding to a 91% retention of its original capacitance. In contrast, the TFP-TPP and TFP-Car COFs exhibited 88.2 and 90.4% retention, respectively. The Ragone plot in Fig. S32 also reveals that the TFP-TPA COF electrode possessed good energy and power densities.

2.4. CO$_2$ adsorption

Fig. 8 displays the CO$_2$ uptakes of our three COFs tested from 0.05 to 1 bar at 298 and 273 K. The spherical TFP-TPA COF exhibited the lowest CO$_2$ uptake capacities: 92 and 183 mg g^{-1} at
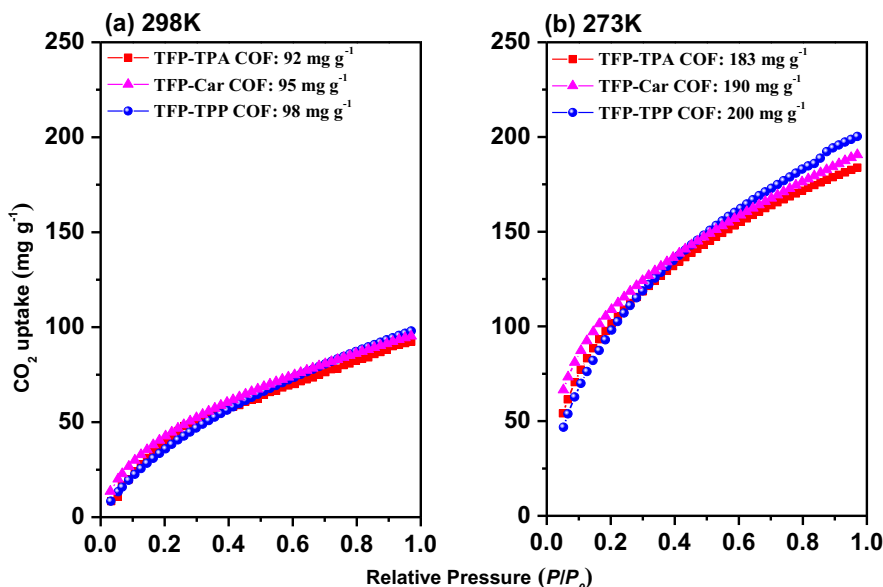
298 K [Fig. 8(a)] and 273 K [Fig. 8(b)], respectively. For the TFP-Car COF, these values were 95 and 190 mg g^{-1}, respectively, and for the TFP-TPP COF they were 98 and 200 mg g^{-1}, respectively. These numbers suggested that there were two factors controlling the CO$_2$ uptake efficiencies of the β-ketoenamine-linked COFs: the degree of planarity of these building monomers and the morphology of these resultant COFs. TFP-Car and TFP-TPP COFs, synthesized from the most-planar monomers Car-3NH$_2$ and TPP-3NH$_2$, respectively, provided CO$_2$ uptake capacities higher than that of TFP-TPA COF, which was synthesized by the least-planar monomer TPA-3NH$_2$.

We attribute this slight difference in the uptake capacities of the TFP-TPA COF and the other two more-planar COFs to the former's spherical morphology, which enhanced the efficiency of the COF to uptake CO$_2$. Moreover, we used the Clausius–Clapeyron equation to calculate the isosteric heat of adsorption (Q_{st}) of these three β-ketoenamine-linked COFs from their CO$_2$ uptake data at 298 and 273 K. By using the low adsorption of CO$_2$ (0.1 mg g^{-1}) as a standard, TFP-TPA, TFP-Car, and TFP-TPP COFs exhibited values of Q_{st} of 44, 49, and 55 kJ mol^{-1}, respectively. These Q_{st} values confirm that the higher-planarity building monomer in the structure of the resultant COF induced a strong quadrupolar interaction with the included CO$_2$ molecules.

In comparison with previously reported β-ketoenamine-linked COFs, our three new TFP-TPA, TFP-Car, and TFP-TPP COFs provide excellent CO$_2$ uptake capacities, especially for the TFP-TPP COF, which exhibited the highest value among them (Table S12). Kandambeth et al. [28] prepared two [3+2] β-ketoenamine-linked COFs, TpPa-1 and TpPa-2, that exhibited CO$_2$ uptake capacities of 154 and 126 mg g^{-1} at 273 K, respectively. Biswal et al. [69] reported a [3+2] β-ketoenamine-linked COF (TpBD) having a CO$_2$ uptake capacity of 85 mg g^{-1} at 273 K. Furthermore, Chandra et al. [70] prepared modified β-ketoenamine-linked COFs with some electron donating and withdrawing substituents to enhancement the CO$_2$ uptake capacity. Their nitro-modified COFs [TpBD-NO$_2$ and TpBD-(NO$_2$)$_2$] exhibited CO$_2$ uptake capacities of 124 and 103 mg g^{-1} at 273 K, respectively, while their fluoro-modified COF (TpBD-F$_4$) exhibited a CO$_2$ uptake capacity of 69 mg g^{-1} at 273 K. Their methyl- and methoxy-modified COFs [TpBD-Me$_2$ and TpBD-(OMe)$_2$] displayed CO$_2$ uptake capacities of 73 and 53 mg g^{-1} at 273 K, respectively. Kaleeswaran et al. [71] synthesized of two [3+3] β-ketoenamine-linked COFs, TAPB-TFPB and iPrTAPB-TFP,

Fig. 8. CO$_2$ uptake capacities of the TFP-TPA (red), TFP-TPP (magenta), and TFP-Car (blue) COFs at (a) 298 and (b) 273 K. (For interpretation of the references to color in this figure legend, the reader is referred to the web version of this article.)

that had CO_2 uptake capacities of 180 and 105 mg g^{-1} at 273 K, respectively. Further, Gomes and Bhaumik [72] prepared of one [3 + 3] β-ketoenamine-linked COF, TRIPTA which exhibited a CO_2 uptake capacity of 570 mg g^{-1} at 273 K. Comparing with imine-based COFs, our synthesized COFs exhibited also excellent CO_2 uptake capacities among them. Almost reported imine-based COFs demonstrated CO_2 uptakes between 20–118 mg g^{-1} at 273 K [57,73], except TRITER-1 COF which reported by Bhaumik and co-workers [74]. It exhibited a CO_2 uptake capacity of 588 mg g^{-1} at 273 K.

3. Conclusion

We have synthesized three novel β-ketoenamine-linked COFs (TFP-COFs) through [3 + 3] polycondensations of TFP-3OHCHO with three tris(aminophenol) derivatives featuring amino, carbazole, and pyridine units, respectively, at their cores and, therefore, different degrees of planarity. These tris(aminophenyl) linkers functioned as novel redox-active moieties in the hexagonal structure of the resulting TFP-COFs. The chemical structures of the prepared TFP-COFs were confirmed by FTIR and solid state NMR spectroscopy. The TFP-COFs possessed high BET surface areas up to 686 m^2 g^{-1} and the excellent crystallinity. The planarity of the tris(aminophenyl) linker controlled the crystallinity of these resultant COFs: increasing the planarity increased the d_{100} value and decreased the π-interlayer distances between the 2D COFs sheets. We tested our β-ketoenamine-linked COFs for their suitability for supercapacitor and gas storage applications. The TFP-COFs exhibited excellent electrochemical efficiencies (up to 291.1 F g^{-1}), due to their conjugated enamine-structures possessing redox-active amino, carbazole, and pyridine units, respectively. The TFP-COFs also possessed excellent CO_2 uptake efficiencies of up to 98 and 200 mg g^{-1} at 298 and 273 K, respectively. The presence of highly planar linkers in the structures of the resultant COFs induced strong quadrupolar interactions with the included CO_2 molecules. This study confirms the importance of monomer planarity on the crystallinity and CO_2 uptake capacity of the corresponding COFs and, hence, their environmental applications. Furthermore, we suspect that these new TFP-COFs—containing new redox-active groups in β-ketoenamine-linked COFs—might be suitable for use in several applications, particularly in energy storage devices.

Acknowledgments

Supplementary material

Supplementary material associated with this article can be found, in the online version, at doi:10.1016/j.jtice.2019.07.016.

References

[1] Khattak AM, Ghazi ZA, Liang B, Khan NA, Iqbal A, et al. A redox-active 2D covalent organic framework with pyridine moieties capable of faradaic energy storage. J Mater Chem A 2016;4:16312–17.

[2] Dutta S, Kim J, Ide Y, Kim JH, Hossain Md SA, Bando Y, Yamauchi Y, Wu KCW. 3D Network of cellulose-based energy storage devices and related emerging applications. Mater Horizons 2017;4:522–45.

[3] Veeramani V, Sivakumar M, Chen SM, Madhu R, Alamri HR, Alothman ZA, Hossain MSA, Chen CK, Yamauchi Y, Miyamoto N, Wu KCW. Lignocellulosic biomass-derived, graphene sheet-like porous activated carbon for electrochemical supercapacitor and catechin sensing. RSC Adv 2017;7:45668–75.

[4] Salunkhe RR, Wang J, Azhar A, Lin J, Malgras V, Bando Y, Zakaria MB, Alshehri AA, Yamauchi Y, Wu KCW. Three-dimensional macroporous graphitic carbon for supercapacitor application. Chem Select 2018;3(16):4522–6.

[5] Kötz R, Carlen M. Principles and applications of electrochemical capacitors. Electrochim Acta 2000;45:2483–98.

[6] Wang G, Zhang L, Zhang J. A review of electrode materials for electrochemical supercapacitors. Chem Soc Rev 2012;41:797–828.

[7] Alabadi A, Yang X, Dong Z, Li Z, Tan B. Nitrogen-doped activated carbons derived from a co-polymer for high supercapacitor performance. J Mater Chem A 2014;2:11697–705.

[8] Wang D, Nai J, Li H, Xu L, Wang Y. A robust strategy for the general synthesis of hierarchical carbons constructed by nanosheets and their application in high performance supercapacitor in ionic liquid electrolyte. Carbon N Y 2019;141:40–9.

[9] Chinnasamy S, Ramasamy J, Rekha GS, Thiyagu S, Subrata M, et al. Indium oxide/carbon nanotube/reduced graphene oxide ternary nanocomposite with enhanced electrochemical supercapacitance. Bull Chem Soc Jpn 2019;92:521–8.

[10] Lin YK, Nguyen VH, Yu JCH, Lee CW, Deng YH, Wu JCS, Wu KCW, Tung KL, Chen CL. Biodiesel production by pervaporation-assisted esterification and pre-esterification using graphene oxide/chitoan composite membranes. J Taiwan Inst Chem E 2017;79:23–30.

[11] Lee MH, Wang SY, Chiang WH, Feng H, Huang TY, Yeh MH, Wu KCW, Ho KC. Platinum nanoparticles decorated graphene nanoribbon with eco-friendly unzipping process. J Taiwan Inst Chem E 2019;96:566–74.

[12] Cheng H-M, Li F. Charge delivery goes the distance. Science 2017;356:582–3.

[13] Wu Z-S, Winter A, Chen L, Sun Y, Turchanin A, et al. Three-dimensional nitrogen and boron Co-doped graphene for high-performance all-solid-state supercapacitors. Adv Mater 2012;24:5130–5.

[14] Wu Z-S, Sun Y, Tan Y-Z, Yang S, Feng X, et al. Three-dimensional graphene-based macro- and mesoporous frameworks for high-performance electrochemical capacitive energy storage. J Am Chem Soc 2012;134:19532–5.

[15] Sui Z-Y, Wang C, Shu K, Yang Q-S, Ge Y, et al. Manganese dioxide-anchored three-dimensional nitrogen-doped graphene hybrid aerogels as excellent anode materials for lithium ion batteries. J Mater Chem A 2015;3:10403–12.

[16] Dutta S, Bhaumik A, Wu KCW. Hierarchically porous carbon derived from polymers and biomass: effect of interconnected pores on energy applications. Energy Environ Sci 2014;7(11):3574–92.

[17] Lin T, Chen I-W, Liu F, Yang C, Bi H, et al. Nitrogen-doped mesoporous carbon of extraordinary capacitance for electrochemical energy storage. Science 2015;350:1508–13.

[18] Hao L, Luo B, Li X, Jin M, Fang Y, et al. Terephthalonitrile-derived nitrogen-rich networks for high performance supercapacitors. Energy Environ Sci 2012;5:9747–51.

[19] Hao L, Ning J, Luo B, Wang B, Zhang Y, et al. Structural evolution of 2D microporous covalent triazine-based framework toward the study of high-performance supercapacitors. J Am Chem Soc 2015;137:219–25.

[20] Su Y, Liu Y, Liu P, Wu D, Zhuang X, et al. Compact coupled graphene and porous polyaryltriazine-derived frameworks as high performance cathodes for lithium-ion batteries. Angew Chem Int Ed 2015;54:1812–16.

[21] Dutta S, Kaneti YV, Hossain Md SA, Shiddiky MJA, Tung KL, Shieh FK, Tsung CK, Wu KCW, Yamauchi Y. Strategies for improving the functionality of zeolitic imidazolate frameworks: tailoring nanoarchitectures for functional applications. Adv Mater 2017;29:1700213.

[22] Veeramani V, Matsagar BM, Yamauchi Y, Badjah AY, Naushad M, Habila M, Wabaidur S, Alothman ZA, Wang ZL, Wu KCW. Metal organic framework derived nickel phosphide/graphitic carbon hybrid for electrochemical hydrogen generation reaction. J Taiwan Inst Chem E 2019;96:634–8.

[23] Wan S, Guo J, Kim J, Ihee H, Jiang D. A photoconductive covalent organic framework: self-condensed arene cubes composed of eclipsed 2D polypyrene sheets for photocurrent generation. Angew Chem Int Ed 2009;48:5439–42.

[24] Ding X, Chen L, Honsho Y, Feng X, Saengsawang O, et al. An n-Channel two-dimensional covalent organic framework. J Am Chem Soc 2011;133:14510–13.

[25] DeBlase CR, Silberstein KE, Truong T-T, Abruña HD, Dichtel WR. β-ketoenamine-linked covalent organic frameworks capable of pseudocapacitive energy storage. J Am Chem Soc 2013;135:16821–4.

[26] DeBlase CR, Hernández-Burgos K, Silberstein KE, Rodríguez-Calero GG, Bisbey RP, et al. Rapid and efficient redox processes within 2D covalent organic framework thin films. ACS Nano 2015;9:3178–83.

[27] Huang N, Zhai L, Coupry DE, Addicoat MA, Okushita K, et al. Multiple-component covalent organic frameworks. Nat Commun 2016;7:12325.

[28] Kandambeth S, Mallick A, Lukose B, Mane MV, Heine T, et al. Construction of crystalline 2D covalent organic frameworks with remarkable chemical (Acid/Base) stability via a combined reversible and irreversible route. J Am Chem Soc 2012;134:19524–7.

[29] Zeng Y, Zou R, Zhao Y. Covalent organic frameworks for CO_2 capture. Adv Mater 2016;28:2855–73.

[30] Waller PJ, Gándara F, Yaghi OM. Chemistry of covalent organic frameworks. Acc Chem Res 2015;48:3053–63.

[31] Shieh FK, Wang SC, Yen CI, Wu CC, Dutta S, Chou LY, Morabito JV, Hu P, Hsu MH, Wu KCW, Tsung CK. Imparting functionality to biocatalysts via embedding enzymes into nanoporous materials by a de novo approach: size-selective sheltering of catalase in metal-organic framework microcrystals. J Am Chem Soc 2015;137(13):4276–9.

[32] Diercks CS, Yaghi OM. The atom, the molecule, and the covalent organic framework. Science 2017;355:1585.

[33] Vinu M, Raja DS, Jiang YC, Liu TY, Xie YY, et al. Effects of structural crystallinity and defects in microporous Al-MOF filled chitosan mixed matrix membranes for pervaporation of water/ethanol mixtures. J Taiwan Inst Chem E 2018;83:143–51.

[34] Côté AP, Benin AI, Ockwig NW, O'Keeffe M, Matzger AJ, et al. Porous, crystalline, covalent organic frameworks. Science 2005;310:1166–70.

[35] Zhou T-Y, Xu S-Q, Wen Q, Pang Z-F, Zhao X. One-step construction of two different kinds of pores in a 2D covalent organic framework. J Am Chem Soc 2014;136:15885–8.

[36] Pang Z-F, Xu S-Q, Zhou T-Y, Liang R-R, Zhan T-G, et al. Construction of covalent organic frameworks bearing three different kinds of pores through the heterostructural mixed linker strategy. J Am Chem Soc 2016;138:4710–13.

[37] Zhang W, Jiang P, Wang Y, Zhang J, Gao Y, et al. Bottom-up approach to engineer a molybdenum-doped covalent-organic framework catalyst for selective oxidation reaction. RSC Adv 2014;4:51544–7.

[38] Fang Q, Gu S, Zheng J, Zhuang Z, Qiu S, et al. 3D Microporous base-functionalized covalent organic frameworks for size-selective catalysis. Angew Chem Int Ed 2014;53:2878–82.

[39] Lin S, Diercks CS, Zhang Y-B, Kornienko N, Nichols EM, et al. Covalent organic frameworks comprising cobalt porphyrins for catalytic CO_2 reduction in water. Science 2015;349:1208–13.

[40] Wan S, Guo J, Kim J, Ihee H, Jiang D. A belt-shaped, blue luminescent, and semiconducting covalent organic framework. Angew Chem Int Ed 2008;47:8826–30.

[41] Xie Y-F, Ding S-Y, Liu J-M, Wang W, Zheng Q-Y. Triazatruxene based covalent organic framework and its quick-response fluorescence-on nature towards electron rich arenes. J Mater Chem C 2015;3:10066–9.

[42] Doonan CJ, Tranchemontagne DJ, Glover TG, Hunt JR, Yaghi OM. Exceptional ammonia uptake by a covalent organic framework. Nat Chem 2010;2:235.

[43] Song J-R, Sun J, Liu J, Huang Z-T, Zheng Q-Y. Thermally/hydrolytically stable covalent organic frameworks from a rigid macrocyclic host. Chem Commun 2014;50:788–91.

[44] Wei H, Chai S, Hu N, Yang Z, Wei L, et al. The microwave-assisted solvothermal synthesis of a crystalline two-dimensional covalent organic framework with high CO_2 capacity. Chem Commun 2015;51:12178–81.

[45] Huang N, Chen X, Krishna R, Jiang D. Two-dimensional covalent organic frameworks for carbon dioxide capture through channel-wall functionalization. Angew Chem Int Ed 2015;54:2986–90.

[46] Ma H, Ren H, Meng S, Yan Z, Zhao H, et al. A 3D microporous covalent organic framework with exceedingly high C_3H_8/CH_4 and C_2 hydrocarbon/CH_4 selectivity. Chem Commun 2013;49:9773–5.

[47] Vyas VS, Vishwakarma M, Moudrakovski I, Haase F, Savasci G, et al. Exploiting noncovalent interactions in an imine-based covalent organic framework for quercetin delivery. Adv Mater 2016;28:8749–54.

[48] Bai L, Phua SZF, Lim WQ, Jana A, Luo Z, et al. Nanoscale covalent organic frameworks as smart carriers for drug delivery. Chem Commun 2016;52:4128–31.

[49] Sun Q, Aguila B, Perman J, Earl LD, Abney CW, et al. Postsynthetically modified covalent organic frameworks for efficient and effective mercury removal. J Am Chem Soc 2017;139:2786–93.

[50] Xu F, Jin S, Zhong H, Wu D, Yang X, et al. Electrochemically active, crystalline, mesoporous covalent organic frameworks on carbon nanotubes for synergistic lithium-ion battery energy storage. Sci Rep 2015;5:8225.

[51] Bai L, Gao Q, Zhao Y. Two fully conjugated covalent organic frameworks as anode materials for lithium ion batteries. J Mater Chem A 2016;4:14106–10.

[52] Colson JW, Dichtel WR. Rationally synthesized two-dimensional polymers. Nat Chem 2013;5:453.

[53] Zha Z, Xu L, Wang Z, Li X, Pan Q, et al. 3D Graphene functionalized by covalent organic framework thin film as capacitive electrode in alkaline media. ACS Appl Mater Inter 2015;7:17837–43.

[54] Romero J, Rodriguez-San-Miguel D, Ribera A, Mas-Ballesté R, Otero TF, et al. Metal-functionalized covalent organic frameworks as precursors of supercapacitive porous N-doped graphene. J Mater Chem A 2017;5:4343–51.

[55] EL-Mahdy AFM, Kuo C-H, Alshehri A, Young C, Yamauchi Y, et al. Strategic design of triphenylamine- and triphenyltriazine-based two-dimensional covalent organic frameworks for CO_2 uptake and energy storage. J Mater Chem A 2018;6:19532–41.

[56] EL-Mahdy AFM, Young C, Kim J, You J, Yamauchi Y, et al. Hollow microspherical and microtubular [3 + 3] carbazole-based covalent organic frameworks and their gas and energy storage applications. ACS Appl Mater Inter 2019;11:9343–54.

[57] Gao Q, Li X, Ning G-H, Xu H-S, Liu C, et al. Covalent organic framework with frustrated bonding network for enhanced carbon dioxide storage. Chem Mater 2018;30:1762–8.

[58] EL-Mahdy AFM, Hung YH, Mansoure TH, Yu HH, Chen T, et al. A hollow microtubular triazine- and benzobisoxazole-based covalent organic framework presenting sponge-like shells that functions as a high-performance supercapacitor. Chem – Asian J 2019;14(9):1429–35.

[59] Chandra S, Kundu T, Dey K, Addicoat M, Heine T, et al. Interplaying intrinsic and extrinsic proton conductivities in covalent organic frameworks. Chem Mater 2016;28:1489–94.

[60] Lou XW, Archer LA, Yang Z. Hollow micro-/nanostructures: synthesis and applications. Adv Mater 2008;20:3987–4019.

[61] Ghosh S, Reches M, Gazit E, Verma S. Bioinspired design of nanocages by self-assembling triskelion peptide elements. Angew Chem Int Ed 2007;46:2002–4.

[62] Kim G, Yang J, Nakashima N, Shiraki T. Highly microporous nitrogen-doped carbon synthesized from azine-linked covalent organic framework and its supercapacitor function. Chem Eur J 2017;23:17504–10.

[63] Hu F, Wang J, Hu S, Li L, Shao W, et al. Engineered fabrication of hierarchical frameworks with tuned pore structure and N,O-Co-doping for high-performance supercapacitors. ACS Appl Mater Inter 2017;9:31940–9.

[64] Su C, He H, Xu L, Zhao K, Zheng C, et al. A mesoporous conjugated polymer based on a high free radical density polytriphenylamine derivative: its preparation and electrochemical performance as a cathode material for li-ion batteries. J Mater Chem A 2017;5:2701–9.

[65] Hsiao S-H, Lin S-W. Electrochemical synthesis of electrochromic polycarbazole films from N-phenyl-3,6-bis(N-carbazolyl)carbazoles. Polym Chem 2016;7:198–211.

[66] Liu W, Ulaganathan M, Abdelwahab I, Luo X, Chen Z, et al. Two-dimensional polymer synthesized via solid-state polymerization for high-performance supercapacitors. ACS Nano 2018;12:852–60.

[67] Deka N, Deka J, Dutta GK. Nitrogen-doped porous carbon derived from carbazole-substituted tetraphenylethylene-based hypercrosslinked polymer for high-performance supercapacitor. ChemistrySelect 2018;3:8483–90.

[68] Zhang D, Gao J, Li Z, He S, Wang J. Synthesis of hierarchically porous carbon spheres by an emulsification-crosslinking method and their application in supercapacitors. RSC Adv 2016;6:54880–8.

[69] Biswal BP, Chandra S, Kandambeth S, Lukose B, Heine T, et al. Mechanochemical synthesis of chemically stable isoreticular covalent organic frameworks. J Am Chem Soc 2013;135:5328–31.

[70] Chandra S, Kandambeth S, Biswal BP, Lukose B, Kunjir SM, et al. Chemically stable multilayered covalent organic nanosheets from covalent organic frameworks via mechanical delamination. J Am Chem Soc 2013;135:17853–61.

[71] Kaleeswaran D, Vishnoi P, Murugavel R. [3+3] imine and β-ketoenamine tethered fluorescent covalent-organic frameworks for CO_2 uptake and nitroaromatic sensing. J Mater Chem C 2015;3:7159–71.

[72] Gomes R, Bhaumik A. A new triazine functionalized luminescent covalent organic framework for nitroaromatic sensing and CO_2 storage. RSC Adv 2016;6:28047–54.

[73] Zhai L, Huang N, Xu H, Chen Q, Jiang D. A backbone design principle for covalent organic frameworks: the impact of weakly interacting units on CO_2 adsorption. Chem Commun 2017;53:4242–5.

[74] Gomes R, Bhanja P, Bhaumik A. A triazine-based covalent organic polymer for efficient CO_2 adsorption. Chem Commun 2015;49:10050–3.